Topological Luttinger semimetallic phase accompanied with surface states realized in silicon

Ying Li, Chi-Ho Cheung, and Gang Xu*
Wuhan National High Magnetic Field Center & School of Physics, Huazhong University of Science and Technology, Wuhan 430074, China

(Received 15 March 2021; revised 14 July 2021; accepted 7 January 2022; published 24 January 2022)

By means of systematically first-principles calculations and model analysis, a complete phase diagram of the body-centered silicon (BC8-Si) via lattice constant a and internal atomic coordinate x is explored, which demonstrates that BC8-Si is a topological Luttinger semimetal (LSM) accompanied with topologically nontrivial surface states, and the electronic properties of BC8-Si can be further tuned to a normal insulator or topological Dirac semimetal by very tiny changing of a and x. These results successfully explain the contradictory transport reports of BC8-Si. More importantly, the topological surface states in the LSM phase fill in the gap between the topological matters and silicon, which provide an opportunity to integrate the topological quantum devices and silicon chips together.

DOI: 10.1103/PhysRevB.105.035136

I. INTRODUCTION

Silicon is the most important material for electronic [1–3] and photovoltaic industry [4–7] due to its excellent electronic properties and mature technology. Especially, almost 90% of electronic chips are equipped based on diamond cubic silicon (DC-Si). Nonetheless, the miniaturization of Si-based chips is facing the end of Moore's law due to the limitation of quantum effects [8]. Searching and devising the next generation of electronic devices are the most urgent and challenging tasks [9,10].

In the past decades, topological matters with nontrivial boundary modes have attracted intensive attentions due to their novel properties [11–15], such as backscattering suppression [16–20], spin-momentum locking [21–24], and non-Abelian braiding [25–27], which are expected to be a significant platform for the next-generation electronic and spintronic devices [28,29]. In order to integrate the topological quantum devices and silicon chips, it is highly desirable to realize the topological boundary modes in silicon [30–39]. However, these two fields have no overlap until now, because DC-Si is well known as a semiconductor without band inversion, which makes it impossible to hold the topological boundary modes.

Fortunately, silicon has more than 13 allotropes [40,41]. Among them, a body-centered cubic structure, named as BC8-Si, was reported to be stabilized under ambient conditions [42–44], but its electronic properties are under debate [45–49]. While previous experiments and calculations suggest that BC8-Si is a semimetal with band overlap [45,47–49], a contrary literature reports that it is a narrow-band-gap semiconductor recently [46]. In particular, the topological properties of BC8-Si have never been studied yet. In this paper, by means of the first-principles calculations, we investigate the electronic and topological properties of BC8-Si systematically, and demonstrate that it is a topological Luttinger semimetal (LSM) with band inversion, on the surface of which, topological surface states can be stabilized. Moreover, our numerical results indicate that the electronic and topological properties of BC8-Si are sensitive to the lattice constant a and internal atomic coordinate x. A complete phase diagram via a and x is explored, which demonstrates that the topological LSM phase of BC8-Si can be tuned to a normal insulator (NI) without band inversion or a topological Dirac semimetal (DSM) by very tiny changing of a and x. Such changing can be achieved by varying the applied pressure during crystal synthesis [50–53]. Our results successfully explain the controversial reports on electronic properties of BC8-Si. More importantly, the topological properties of BC8-Si fill in the gap between the topological matters and silicon, which provides an opportunity to integrate the next-generation electronic quantum devices and silicon chips.

II. CRYSTAL STRUCTURE AND METHODOLOGY

As shown in Fig. 1(a), BC8-Si adopts the body-centered cubic lattice with space group Ia-3 (No. 206), where the lattice constant a equals 6.636 Å and Si atoms are located at 16c Wyckoff position with coordinate $x = 0.1003$ [51,52]. These most reported experimental crystal parameters are used in our calculations, otherwise they will be explicitly pointed out. Compared with DC-Si, Si atoms form a slightly distorted tetrahedral structure with two types Si-Si distance $A = 2.305$ Å and $B = 2.391$ Å in BC8-Si. The first Brillouin zone (BZ) of the primitive cell and its projection on the (001) surface of the unit cell are displayed in Fig. 1(b). Our first-principles calculations are performed by the Vienna *ab initio* simulation package [54,55] with the projected augmented wave method [56]. The energy cutoff is set as 400 eV, and $7 \times 7 \times 7$ k meshes are adopted. Perdew-Burke-Ernzerhof type of the exchange-correlation potential [57], and Heyd-Scuseria-Ernzerhof (HSE06) hybrid functional [58] are used to obtain accurate electronic structures. The accuracy of HSE06 is double checked by the quasiparticle self-consistent GW_0 method [59]. As shown in the Supplemental Material (SM) [60], detailed comparisons reveal that the electronic structures

*gangxu@hust.edu.cn

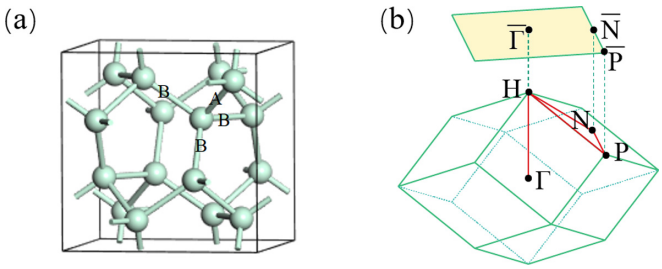

FIG. 1. (a) Unit cell of the body-centered cubic silicon, BC8-Si, with space group $Ia-3$ (No. 206), where two types of Si-Si bond length A = 2.305 Å, B = 2.391 Å are labeled. (b) BZ of the primitive cell with high-symmetry path and its projection on the (001) surface of the unit cell.

of BC8-Si have a slightly functional dependency. Considering that HSE06 with mixing factor 0.35 has been confirmed to well reproduce the experimentally observed band dispersion of BC8-Si in Ref. [46], we would adopt it to study the main results in our paper. Spin-orbit coupling (SOC) interaction is considered consistently. Symmetry preserving Wannier functions are constructed by the Wannier90 package [61]. The surface states are calculated by iterative Green's function method as implemented in the WannierTools package [62].

III. LUTTINGER SEMIMETAL

The electronic configuration of Si atom is $3s^2 3p^2$. Because each Si atom is tetrahedrally connected with the other four Si atoms, the main chemical bonding in BC8-Si is sp^3 hybridization [63], which is similar to the chemical bonding in DC-Si [64]. As a result, the calculated band structures in Fig. 2(a) show that the sp^3 bonding states are almost fully occupied and contribute to the valence bands, while the sp^3 antibonding states are almost empty and form conduction bands. However, different from semiconductor DC-Si, one antibonding state $|ab\rangle^-$ with H_1^- irreducible representation (IRR) in BC8-Si is lower than its bonding states $|b_1\rangle^+$, $|b_2\rangle^+$, $|b_3\rangle^+$ with H_4^+ IRR at H point as shown in the inset of Figs. 2(a) and 2(b), where the superscript $+/-$ denotes parity. Then the band inversion in BC8-Si makes it a semimetal, which agree with previous experimental and theoretical studies well [45,47–49]. Due to the presence of inversion symmetry (I) and time reversal symmetry ($\mathcal{T}$), each band in BC8-Si is doubly degenerate at every momentum k, which means that the band touching at Fermi level (E_F) is fourfold degenerate. Furthermore, the dispersion around the fourfold degenerate node is always parabolic as shown in Fig. 2(b), which indicates that BC8-Si is a LSM.

IV. MODEL ANALYSIS

To understand the low energy band structures in BC8-Si shown in Fig. 2(b), we construct a $k\cdot p$ model at H point, where the vector group is T_h with generators C_2^{100}, C_3^{111} and I. By including the SOC effect, the basis can be written in

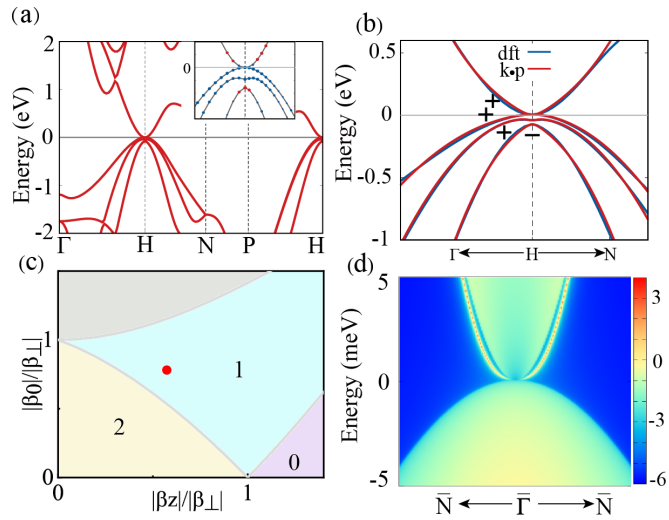

FIG. 2. (a) The calculated band structures of BC8-Si, red and blue circles indicate the projection to the antibonding states and bonding states, respectively. (b) The fitted band structures by the eight-band $k\cdot p$ model and first-principles calculations. (c) The topological phase diagram of the 2D nodal semimetal in the (β_0, β_z) plane, where the parameters of BC8-Si's reduction is marked by the red circle. (d) The calculated LDOS illustrates the topological surface mode on the (001) surface of the unit cell.

the $|J, J_z\rangle$ representation, where J represents the total angular momentum and J_z represents its z-direction component. Based on the chemical bonding analysis, we define the new basis as $\Psi[|\frac{3}{2},\frac{3}{2}\rangle^+ = \frac{1}{\sqrt{2}}|-(b_1+ib_2),\uparrow\rangle^+, |\frac{3}{2},\frac{1}{2}\rangle^+ = \frac{1}{\sqrt{6}}|(b_1+ib_2),\downarrow\rangle^+ - \sqrt{\frac{2}{3}}|b_3,\uparrow\rangle^+, \quad |\frac{1}{2},\frac{1}{2}\rangle^+ = \frac{1}{\sqrt{3}}|-(b_1+ib_2),\downarrow\rangle^+ - \frac{1}{\sqrt{3}}|b_3,\uparrow\rangle^+, |\frac{1}{2},\frac{1}{2}\rangle^- = |iab,\uparrow\rangle^-]$, and $\mathcal{T}\Psi$. The full Hamiltonian takes the form (see more details in Sec. II of SM [60])

$$H = \begin{bmatrix} h_{\uparrow\uparrow}(k) & h_{\uparrow\downarrow}(k) \\ -h^*_{\uparrow\downarrow}(-k) & h^*_{\uparrow\uparrow}(-k) \end{bmatrix},$$

$$h_{\uparrow\uparrow}(k) = \begin{bmatrix} M_1(k) & \frac{t_6 k_- k_z}{\sqrt{3}} & \frac{t_6 k_- k_z}{\sqrt{6}} & \frac{t_5 k_-}{\sqrt{2}} \\ \frac{t_6 k_+ k_z}{\sqrt{3}} & M_0(k) & -V_2(k) & \sqrt{\frac{2}{3}} t_5 k_z \\ \frac{t_6 k_+ k_z}{\sqrt{6}} & -V_2(k) & M_2(k) & \frac{t_5 k_z}{\sqrt{3}} \\ \frac{t_5 k_+}{\sqrt{2}} & \sqrt{\frac{2}{3}} t_5 k_z & \frac{t_5 k_z}{\sqrt{3}} & M_3(k) \end{bmatrix},$$

$$h_{\uparrow\downarrow}(k) = \begin{bmatrix} 0 & V_1(k) & -\sqrt{2}V_1(k) & 0 \\ -V_1(k) & 0 & \frac{t_6 k_- k_z}{\sqrt{2}} & -\frac{t_5 k_-}{\sqrt{6}} \\ \sqrt{2}V_1(k) & -\frac{t_6 k_- k_z}{\sqrt{2}} & 0 & \frac{t_5 k_-}{\sqrt{3}} \\ 0 & -\frac{t_5 k_-}{\sqrt{6}} & \frac{t_5 k_-}{\sqrt{3}} & 0 \end{bmatrix}, \quad (1)$$

where

$$M_0(k) = E_b + \lambda + \frac{1}{6}\left[(t_1+4t_2+t_3)k_x^2 + (4t_1+t_2+t_3)k_y^2 + (t_1+t_2+4t_3)k_z^2\right],$$

$$M_1(k) = E_b + \lambda + \frac{1}{2}\left[(t_1+t_3)k_x^2 + (t_2+t_3)k_y^2 + (t_1+t_2)k_z^2\right],$$

TABLE I. Fitted parameters of $k \cdot p$ Hamiltonian at H point.

t_1 eV Å^2	t_2 eV Å^2	t_3 eV Å^2	t_4 eV Å^2	t_5 eV Å	t_6 eV Å^2	E_b eV	E_{ab} eV	λ eV
−4.638	−8.636	−20.098	11.662	−2.413	−8.5	0.0	−0.063	0.015

$$
\begin{aligned}
M_2(k) &= E_b - 2\lambda + \frac{1}{3}(t_1 + t_2 + t_3)\big(k_x^2 + k_y^2 + k_z^2\big),\\
M_3(k) &= E_{ab} + t_4\big(k_x^2 + k_y^2 + k_z^2\big),\\
V_1(k) &= \frac{1}{2\sqrt{3}}\big[(-t_1+t_2)k_z^2+(-t_2+t_3)k_y^2 + (t_1 - t_3)k_x^2 + 2it_6k_xk_y\big],\\
V_2(k) &= \frac{1}{3\sqrt{2}}\big[(t_1 + t_2 - 2t_3)k_z^2 + (t_1 - 2t_2 + t_3)k_x^2 + (-2t_1 + t_2 + t_3)k_y^2\big],\\
k_\pm &= k_x \pm ik_y.
\end{aligned}
$$

E_b and E_{ab} are the on-site energies of bonding and antibonding states, respectively. t_1, t_2, t_3, and t_4 are the mass terms in bonding and antibonding subspace. t_5 is the coupling between the bonding and antibonding subspaces, while t_6 is the coupling within the bonding subspace. λ is the atomic SOC strength. We use the effective model to fit the first-principles calculations and tabulate the fitted parameters in Table I. The fitted band structures (red) agree with the first-principles calculations very well, as plotted in Figs. 2(b) and S3. The Hamiltonian in Eq. (1) explicitly shows that the energy difference between $|J = \frac{1}{2}\rangle^-$ and $|J = \frac{3}{2}\rangle^+$ at H point can be described as $\Delta = E_{ab} - E_b - \lambda$. According to the fitted parameters list in Table I, we get Δ= –78 meV <0, which means that the band inversion is well reproduced by our model and parameters. One important consequence of the band inversion is that the fourfold degenerate node formed by the $|J = \frac{3}{2}\rangle^+$ states is left at the E_F exactly. Since k^2 is the leading order in the $|J = \frac{3}{2}\rangle^+$ subspace, the band dispersion around the fourfold degenerate node are always parabolic. These results theoretically clarify that BC8-Si is a LSM with band inversion.

V. TOPOLOGICAL CHARACTERS

Maxim Kharitonov *et al.* have reported that the four-band 3-dimensional LSM is topological and can exhibit surface states, if its 2-dimensional (2D) reductions to some planes in momentum space passing the quadratic node are topologically nontrivial [65]. The topological properties of the reduced 2D nodal semimetal are determined by the phase diagram in $(\frac{|\beta_0|}{|\beta_\perp|}, \frac{|\beta_z|}{|\beta_\perp|})$ parameter plane, as shown in Fig. 2(c) [65]. Here, $\beta_\perp$ is the coefficient of the Pauli matrix $\sigma_{x,y}$ characterizing a chiral symmetric of 2D LSM, and β_0, β_z are the coefficients of σ_0 and σ_z describing the breaking of the chiral symmetry. In Fig. 2(c), the gray region $|\beta_0| > \sqrt{|\beta_\perp|^2 + \beta_z^2}$ means that the system is no longer a semimetal, the pink region labeled by 0 is trivial semimetal, the blue and yellow region labeled by topological number 1 and 2 are the nontrivial LSM accompanied by one and two edge states, respectively.

To explore the topological properties of BC8-Si, the eight-band model in Eq. (1) is downfolded to four-band Hamiltonian by perturbation theory [66]. The details of downfolding are shown in the Sec. III of SM [60]. Under the basis of $|\frac{3}{2}, \frac{3}{2}\rangle^+$, $|\frac{3}{2}, \frac{1}{2}\rangle^+$, $|\frac{3}{2}, -\frac{3}{2}\rangle^+$ and $|\frac{3}{2}, -\frac{1}{2}\rangle^+$, a new Hamiltonian describing the low energy physics of LSM in BC-8 Si is written as

$$
\begin{aligned}
H_{4\times4} &= H_0 + H_c,\\
H_0 &= \frac{1}{2}(M_0(k) + M_1(k))\tau_0\sigma_0 + \frac{1}{2}(M_1(k) + M_0(k))\tau_0\sigma_z\\
&\quad - Re(V_1(k))\tau_y\sigma_y - Im(V_1(k))\tau_x\sigma_y\\
&\quad + \frac{t_6}{\sqrt{3}}(k_xk_z\tau_0\sigma_x + k_yk_z\tau_z\sigma_y),\\
H_c &= \frac{t_5^2}{-\Delta}\Bigg[\frac{1}{2}(M_0'(k) + M_1'(k))\tau_0\sigma_0\\
&\quad + \frac{1}{2}(M_1'(k) + M_0'(k))\tau_0\sigma_z\\
&\quad - \frac{1}{2\sqrt{3}}[-k_/^2\tau_y\sigma_y + 2k_xk_y\tau_x\sigma_y]\\
&\quad + \frac{1}{\sqrt{3}}(k_xk_z\tau_0\sigma_x + k_yk_z\tau_z\sigma_y)\Bigg].
\end{aligned}
\tag{2}
$$

τ_0 and σ_0 are the 2×2 identity matrices, $\tau_{x,y,z}$ and $\sigma_{x,y,z}$ represent the orbital and spin space, respectively. H_0 is the $|J = \frac{3}{2}\rangle^+$ subspace of the eight-band model in Eq. (1), H_c is the influence part from $|J_z = \pm\frac{1}{2}\rangle^-$ states, in which $k_/^2 = k_x^2 + k_y^2$, $M_0'(k) = \frac{1}{6}k_/^2 + \frac{2}{3}k_z^2$, $M_1'(k) = \frac{1}{2}k_/^2$.

Taking a similar procedure as in Ref. [65], one can reduce Eq. (2) into two 2×2 2D models by assuming $k_z = 0$. One of them under the basis of $|\frac{3}{2}, \frac{3}{2}\rangle^+$, $|\frac{3}{2}, -\frac{1}{2}\rangle^+$ is written as

$$
H_{2\times2} = \begin{bmatrix} \frac{\alpha+\gamma}{4}k_/^2 & \frac{\omega+\eta}{4\sqrt{3}}k_-^2 \\ \frac{\omega+\eta}{4\sqrt{3}}k_+^2 & \frac{\delta+\zeta}{12}k_/^2 \end{bmatrix} + \frac{t_5^2}{-\Delta}\begin{bmatrix} \frac{k_/^2}{2} & -\frac{k_-^2}{2\sqrt{3}} \\ -\frac{k_+^2}{2\sqrt{3}} & \frac{1}{6}k_/^2 \end{bmatrix} + H_{\text{anis}},
\tag{3}
$$

with $\alpha = t_1 + t_3$, $\gamma = t_2 + t_3$, $\delta = t_1 + 4t_2 + t_3$, $\zeta = 4t_1 + t_2 + t_3$, $\omega = -t_2 + t_3$, $\eta = t_1 - t_3$. The other Hamiltonian is its conjugate under the basis of $|\frac{3}{2}, -\frac{3}{2}\rangle^+$, $|\frac{3}{2}, \frac{1}{2}\rangle^+$. Thus, we can

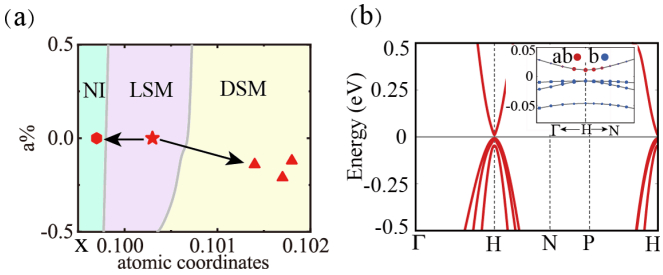

FIG. 3. (a) Phase diagram of BC8-Si under strain in the range of (–0.5%, +0.5%). (b) The band structures of NI, the inset is the projected band structures around H point, red and blue circles indicate the projection to the antibonding states and bonding states, respectively.

just study the coefficients of Eq. (3) separately to determine the topological properties of the 2D quadratic model (see more details in Sec. IV of SM [60]). With parameters given in Table I, the calculated $\frac{|\beta_0|}{|\beta_\perp|}$, $\frac{|\beta_z|}{|\beta_\perp|}$ are 0.7804 and 0.5733, which corresponds to a phase point as marked by a red circle in Fig. 2(c) that belongs to the nontrivial region with topological number 1. Our numerical results strongly imply that BC8-Si is a topological LSM, and one surface state is anticipated on the surface. To prove that, the maximally localized Wannier functions for antibonding and bonding states are constructed. The local density of states (LDOS) on the (001) surface are calculated based on the maximally localized Wannier functions by using Green's function method. As shown in Fig. 2(d), one topological surface state as a parabola going upwards at $\bar{\Gamma}$ presents clearly, which confirms the topologically nontrivial characters of BC8-Si. Such parabolic type of surface states are different from the surface states in other topological materials such as topological insulator or topological DSM [67,68]. We notice that the same topological surface states can also be observed in (100) and (010) plane due to the presence of C_3^{111}. Further angle-resolved photoemission spectroscopy experiment is highly desirable to verify such topological surface states in BC8-Si.

VI. PHASE DIAGRAM

Since it has been reported that the electronic property of BC8-Si is sensitive to lattice constant a and internal atomic coordinate x [45,46], we further investigate their impacts on the band structures and topological properties by first-principles calculations. The calculated phase diagram with various a and x consists of three subregions, NI, topological LSM and DSM, labeled by different colors in Fig. 3(a). Our results demonstrate that the electronic properties of BC8-Si are more sensitive to the atomic coordinate x. In general, pressure will shorten the atomic distance and compress the lattice parameters by increasing x and compressing a concurrently [69]. We have investigated many reported structure parameters of BC8-Si, and found that they are slightly different. For the most reported parameters in atmosphere [51,52], it falls into the topological LSM phase as marked by the red star in Fig. 3(a). Under the pressure of 2 ∼ 10 Gpa, BC8-Si becomes topological DSM with $a = 6.6218 \sim 6.6276$ Å and $x = 0.1014 \sim 0.1018$ [48,53] as marked by red triangles in

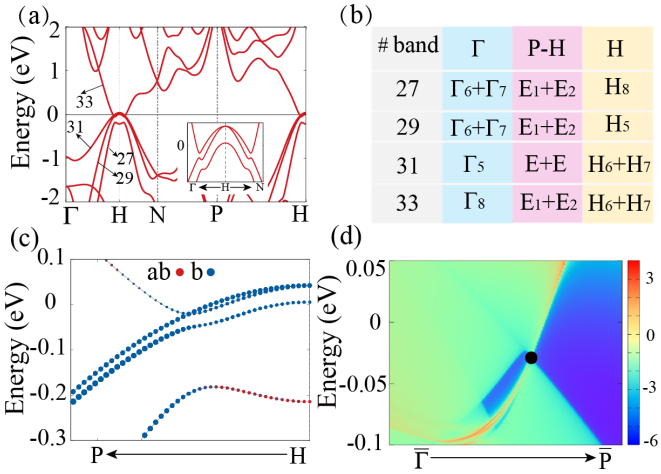

# band	Γ	P-H	H
27	$\Gamma_6+\Gamma_7$	E_1+E_2	H_8
29	$\Gamma_6+\Gamma_7$	E_1+E_2	H_5
31	Γ_5	E+E	H_6+H_7
33	Γ_8	E_1+E_2	H_6+H_7

FIG. 4. (a) Band structures of topological DSM. (b) IRRs of DSM bands around E_F. (c) Enlarged projected band structures along $P-H$ around the Dirac point. (d) The calculated LDOS of DSM on its (001) surface of the unit cell, where black dot represents location of projected Dirac point.

Fig. 3(a). In contrast, it falls into NI region with enlarging a and decreasing x as colored by turquoise. This means that various electronic states of BC8-Si illustrated in Fig. 3(a) can be obtained by applying external force, as discussed in α-Sn [70] and Cu_2Se [71].

VII. NORMAL INSULATOR

Actually, different structural parameters, and even different electronic states can be accessed by varying the synthesis conditions [50–52,69]. Previous optical spectroscopy and electrical conductivity measurements [46] indeed show that BC8-Si fall into the semiconducting phase with an ultra narrow direct band gap, which corresponds well to the NI phase in Fig. 3(a). In Fig. 3(b), by using $a = 6.636$ Å and $x = 0.0997$ as marked by a red hexagon in Fig. 3(a), we plot the calculated band structures as a representation of the NI state, which give rise to a direct band gap of 5 meV at H point. Different from the topological LSM phase, the energy difference Δ is positive in the NI phase, which is clearly illustrated by the orbital projections shown in the inset of Fig. 3(b). Finally, we would like to emphasize that the coordinate x only changes about 0.6% from the topological LSM in Fig. 2 to this NI phase, which is totally feasible by changing the applied pressure during crystal synthesis.

VIII. DIRAC SEMIMETAL

We next discuss the DSM phase, which can be obtained by applying a compressive strain to the topological LSM phase. The internal coordinate $x = 0.1018$ is adopted, which has been reported in another experiment [53]. The calculated band structures and corresponding IRRs of DSM are shown in Figs. 4(a) and 4(b). As shown in Figs. 4(a) and 4(c), the band inversion Δ is obviously enhanced to –256 meV in DSM, comparing to –78 meV in LSM phase. This makes the fourfold degenerate node lift above the E_F. As a result, the

low energy physics is determined by the crossing between $|J_z = \pm\frac{3}{2}\rangle^+$ and $|J_z = \pm\frac{1}{2}\rangle^-$ states. In general, the SOC interaction would open a hybridization gap at all the crossing point of $|J_z = \pm\frac{3}{2}\rangle^+$ and $|J_z = \pm\frac{1}{2}\rangle^-$ states as shown in the inset of Fig. 4(a). However, on the $H - P$ path, due to the presence of C_3^{111}, $|J_z = \pm\frac{3}{2}\rangle^+$ states have the $E + E$ [72] IRRs, while $|J_z = \pm\frac{1}{2}\rangle^-$ states have $E_1 + E_2$ [72] IRRs. They could cross each other exactly and form a Dirac point close to the E_F as shown in Fig. 4(c). According to the above discussions, the DSM phase in BC8-Si is similar to that of Na_3Bi, both of them are protected by C_3, I and $\mathcal{T}$ [68]. Therefore, Fermi arcs formed by the topological surface states would be expected on its surface. By constructed the maximally localized Wannier functions, we carry out the Green's function calculations on the semi-infinite (001) surface of the unit cell, and plot the corresponding LDOS in Figs. 4(d) and S4, which evidently show two Fermi arcs originated from the projected Dirac point as have been reported in other DSMs [14,68]. We also calculate the LDOS on the (111) surface of the unit cell, and display them in Fig. S5. However, it is more difficult to distinguish the Fermi arcs and their connection, because the Dirac points and the Fermi arcs are hybridized drastically with bulk bands (see more details in Sec. V of SM [60]).

IX. CONCLUSIONS

The electronic and topological properties of BC8-Si are explored by the first-principles calculations and model analysis. It demonstrates that BC8-Si is a topological LSM characterized by the band inversion at H point and one quadratic node is located at E_F exactly, which can hold the stabilized topological surface state on its (001) surface of the unit cell. Our calculations further suggest that LSM can be tuned to a NI or topological DSM by tiny changing of the crystal parameters, which can be achieved by the variation of the applied pressure during crystal synthesis. These results can well explain the previous contrary reports on the electronic properties of BC8-Si. More importantly, the topological surface states in BC8-Si could be a good connection between the topological quantum devices and silicon chips, which will stimulate more efforts on the promising electronic devices.

ACKNOWLEDGMENTS

This work was supported by the National Key Research and Development Program of China (Grant No. 2018YFA0307000), and the National Natural Science Foundation of China (Grant No. 11874022).

[1] R. N. Noyce, Semiconductor device-and-lead structure, Reprint of U.S. Patent 2,981,877 (Issued April 25, 1961. Filed July 30, 1959), IEEE Solid-State Circuits Soc. Newsletter **12**, 34 (2007).

[2] J. S. Kilby, Miniaturized electronic circuits [US Patent No. 3,138,743], IEEE Solid-State Circuits Soc. Newsletter **12**, 44 (2007).

[3] C. Kittel, P. McEuen, and P. McEuen, *Introduction to Solid State Physics*, 8th ed. (John Wiley, Hoboken, NJ, 1996).

[4] D. E. Carlson and C. R. Wronski, Amorphous silicon solar cell, Appl. Phys. Lett. **28**, 671 (1976).

[5] M. A. Green, *Solar Cells: Operating Principles, Technology, and System Applications* (Office of Scientific and Technical Information, Oak Ridge, TN, 1982).

[6] M. A. Green, E. D. Dunlop, J. Hohl-Ebinger, M. Yoshita, N. Kopidakis, and A. W. Ho-Baillie, Solar cell efficiency tables (Version 55), Prog. Photovolt: Res. Appl. **28**, 3 (2020).

[7] S. Botti, J. A. Flores-Livas, M. Amsler, S. Goedecker, and M. A. L. Marques, Low-energy silicon allotropes with strong absorption in the visible for photovoltaic applications, Phys. Rev. B **86**, 121204(R) (2012).

[8] H. N. Khan, D. A. Hounshell, and E. R. Fuchs, Science and research policy at the end of Moore's law, Nat. Electron **1**, 14 (2018).

[9] B. Radisavljevic, A. Radenovic, J. Brivio, V. Giacometti, and A. Kis, Single-layer MoS_2 transistors, Nat. Nanotechnol. **6**, 147 (2011).

[10] D. Hsieh, D. Qian, L. Wray, Y. Xia, Y. S. Hor, R. J. Cava, and M. Z. Hasan, A topological Dirac insulator in a quantum spin Hall phase, Nature (London) **452**, 970 (2008).

[11] C. L. Kane and E. J. Mele, Quantum Spin Hall Effect in Graphene, Phys. Rev. Lett. **95**, 226801 (2005).

[12] X.-L. Qi and S.-C. Zhang, Topological insulators and superconductors, Rev. Mod. Phys. **83**, 1057 (2011).

[13] G. Xu, H. Weng, Z. Wang, X. Dai, and Z. Fang, Chern Semimetal and the Quantized Anomalous Hall Effect in $HgCr_2Se_4$, Phys. Rev. Lett. **107**, 186806 (2011).

[14] G. Hua, S. Nie, Z. Song, R. Yu, G. Xu, and K. Yao, Dirac semimetal in type-IV magnetic space groups, Phys. Rev. B **98**, 201116(R) (2018).

[15] J. Zou, Z. He, and G. Xu, The study of magnetic topological semimetals by first principles calculations, npj Comput. Mater. **5**, 96 (2019).

[16] M. Büttiker, Absence of backscattering in the quantum Hall effect in multiprobe conductors, Phys. Rev. B **38**, 9375 (1988).

[17] B. Yan and S.-C. Zhang, Topological materials, Rep. Prog. Phys. **75**, 096501 (2012).

[18] G. Xu, J. Wang, C. Felser, X.-L. Qi, and S.-C. Zhang, Quantum anomalous Hall effect in magnetic insulator heterostructure, Nano Lett. **15**, 2019 (2015).

[19] G. Xu, B. Lian, and S.-C. Zhang, Intrinsic Quantum Anomalous Hall Effect in the Kagome Lattice $Cs_2LiMn_3F_{12}$, Phys. Rev. Lett. **115**, 186802 (2015).

[20] S. A. Hassani Gangaraj, C. Valagiannopoulos, and F. Monticone, Topological scattering resonances at ultralow frequencies, Phys. Rev. Research **2**, 023180 (2020).

[21] D. Hsieh, Y. Xia, D. Qian, L. Wray, J. Dil, F. Meier, J. Osterwalder, L. Patthey, J. Checkelsky, N. P. Ong *et al.*, A tunable topological insulator in the spin helical Dirac transport regime, Nature (London) **460**, 1101 (2009).

[22] K. Gotlieb, C.-Y. Lin, M. Serbyn, W. Zhang, C. L. Smallwood, C. Jozwiak, H. Eisaki, Z. Hussain, A. Vishwanath, and A. Lanzara, Revealing hidden spin-momentum locking in a high-temperature cuprate superconductor, Science **362**, 1271 (2018).

[23] H. Zhang, C.-X. Liu, and S.-C. Zhang, Spin-Orbital Texture in Topological Insulators, Phys. Rev. Lett. **111**, 066801 (2013).

[24] S. Nie, G. Xu, F. B. Prinz, and S.-c. Zhang, Topological semimetal in honeycomb lattice LnSI, Proc. Natl. Acad. Sci. USA **114**, 10596 (2017).

[25] C. Nayak, S. H. Simon, A. Stern, M. Freedman, and S. Das Sarma, Non-Abelian anyons and topological quantum computation, Rev. Mod. Phys. **80**, 1083 (2008).

[26] X. Wu, R.-X. Zhang, G. Xu, J. Hu, and C.-X. Liu, In the pursuit of Majorana modes in iron-based high-T_c superconductors, in *Memorial Volume for Shoucheng Zhang* (World Scientific, Singapore, 2022), Chap. 3, pp. 35–60.

[27] G. Xu, B. Lian, P. Tang, X.-L. Qi, and S.-C. Zhang, Topological Superconductivity on the Surface of Fe-Based Superconductors, Phys. Rev. Lett. **117**, 047001 (2016).

[28] X.-L. Qi, R. Li, J. Zang, and S.-C. Zhang, Inducing a magnetic monopole with topological surface states, Science **323**, 1184 (2009).

[29] I. Garate and M. Franz, Inverse Spin-Galvanic Effect in the Interface between A Topological Insulator and a Ferromagnet, Phys. Rev. Lett. **104**, 146802 (2010).

[30] C.-C. Liu, W. Feng, and Y. Yao, Quantum Spin Hall Effect in Silicene and Two-Dimensional Germanium, Phys. Rev. Lett. **107**, 076802 (2011).

[31] H. Pan, Z. Li, C.-C. Liu, G. Zhu, Z. Qiao, and Y. Yao, Valley-Polarized Quantum Anomalous Hall Effect in Silicene, Phys. Rev. Lett. **112**, 106802 (2014).

[32] X.-T. He, E.-T. Liang, J.-J. Yuan, H.-Y. Qiu, X.-D. Chen, F.-L. Zhao, and J.-W. Dong, A silicon-on-insulator slab for topological valley transport, Nat. Commun. **10**, 872 (2019).

[33] M. Zare, F. Parhizgar, and R. Asgari, Topological phase and edge states dependence of the RKKY interaction in zigzag silicene nanoribbon, Phys. Rev. B **94**, 045443 (2016).

[34] Z. Liu, H. Xin, L. Fu, Y. Liu, T. Song, X. Cui, G. Zhao, and J. Zhao, All-silicon topological semimetals with closed nodal line, J. Phys. Chem. Lett. **10**, 244 (2018).

[35] F. Cargnoni, C. Gatti, E. May, and D. Narducci, Geometrical reconstructions and electronic relaxations of silicon surfaces. I. An electron density topological study of H-covered and clean Si (111)(1 × 1) surfaces, J. Chem. Phys. **112**, 887 (2000).

[36] S. M. Kang, M. K. Siddiqui, N. A. Rehman, M. Naeem, and M. H. Muhammad, Topological properties of 2-dimensional silicon-carbons, IEEE Access **6**, 59362 (2018).

[37] A. Shtyk and C. Chamon, Topological electronic properties of silicon, Phys. Rev. B **102**, 195125 (2020).

[38] C. Ojeda-Aristizabal, M. Fuhrer, N. P. Butch, J. Paglione, and I. Appelbaum, Towards spin injection from silicon into topological insulators: Schottky barrier between Si and Bi_2Se_3, Appl. Phys. Lett. **101**, 023102 (2012).

[39] M. Tahir and U. Schwingenschlögl, Valley polarized quantum Hall effect and topological insulator phase transitions in silicene, Sci. Rep. **3**, 1075 (2013).

[40] G. J. Ackland, High-pressure phases of group IV and III-V semiconductors, in *High-Pressure Surface Science and Engineering* (CRC Press, New York, 2019).

[41] B. Haberl, T. A. Strobel, and J. E. Bradby, Pathways to exotic metastable silicon allotropes, Appl. Phys. Rev. **3**, 040808 (2016).

[42] R. Wentorf and J. Kasper, Two new forms of silicon, Science **139**, 338 (1963).

[43] J. Crain, G. J. Ackland, J. R. Maclean, R. O. Piltz, P. D. Hatton, and G. S. Pawley, Reversible pressure-induced structural transitions between metastable phases of silicon, Phys. Rev. B **50**, 13043 (1994).

[44] R. O. Piltz, J. R. Maclean, S. J. Clark, G. J. Ackland, P. D. Hatton, and J. Crain, Structure and properties of silicon XII: A complex tetrahedrally bonded phase, Phys. Rev. B **52**, 4072 (1995).

[45] B. D. Malone, J. D. Sau, and M. L. Cohen, Ab initio survey of the electronic structure of tetrahedrally bonded phases of silicon, Phys. Rev. B **78**, 035210 (2008).

[46] H. Zhang, H. Liu, K. Wei, O. O. Kurakevych, Y. Le Godec, Z. Liu, J. Martin, M. Guerrette, G. S. Nolas, and T. A. Strobel, BC8 Silicon (Si-III) is a Narrow-Gap Semiconductor, Phys. Rev. Lett. **118**, 146601 (2017).

[47] J. Besson, E. Mokhtari, J. Gonzalez, and G. Weill, Electrical Properties of Semimetallic Silicon III and Semiconductive Silicon IV at Ambient Pressure, Phys. Rev. Lett. **59**, 473 (1987).

[48] A. Wosylus, H. Rosner, W. Schnelle, and U. Schwarz, Crystal structure refinement and electronic properties of Si (cI16), Z. Anorg. Allg. Chem. **635**, 700 (2009).

[49] B. G. Pfrommer, M. Côté, S. G. Louie, and M. L. Cohen, *Ab initio* study of silicon in the R8 phase, Phys. Rev. B **56**, 6662 (1997).

[50] J. Crain, R. Piltz, G. Ackland, S. Clark, M. Payne, V. Milman, J. Lin, P. Hatton, and Y. Nam, Tetrahedral structures and phase transitions in III-V semiconductors, Phys. Rev. B **50**, 8389 (1994).

[51] J. Z. Hu, L. D. Merkle, C. S. Menoni, and I. L. Spain, Crystal data for high-pressure phases of silicon, Phys. Rev. B **34**, 4679 (1986).

[52] J. Kasper and S. Richards, The crystal structures of new forms of silicon and germanium, Acta Crystallogr. **17**, 752 (1964).

[53] O. O. Kurakevych, Y. Le Godec, W. A. Crichton, J. Guignard, T. A. Strobel, H. Zhang, H. Liu, C. Coelho Diogo, A. Polian, and N. Menguy, Synthesis of bulk BC8 silicon allotrope by direct transformation and reduced-pressure chemical pathways, Inorg. Chem. **55**, 8943 (2016).

[54] G. Kresse and J. Furthmüller, Efficient iterative schemes for *ab initio* total-energy calculations using a plane-wave basis set, Phys. Rev. B **54**, 11169 (1996).

[55] G. Kresse and J. Furthmüller, Efficiency of ab-initio total energy calculations for metals and semiconductors using a plane-wave basis set, Comput. Mater. Sci. **6**, 15 (1996).

[56] P. E. Blöchl, Projector augmented-wave method, Phys. Rev. B **50**, 17953 (1994).

[57] J. P. Perdew, K. Burke, and M. Ernzerhof, Generalized Gradient Approximation Made Simple, Phys. Rev. Lett. **77**, 3865 (1996).

[58] J. Heyd, G. E. Scuseria, and M. Ernzerhof, Hybrid functionals based on a screened Coulomb potential, J. Chem. Phys. **118**, 8207 (2003).

[59] L. Hedin, New method for calculating the one-particle Green's function with application to the electron-gas problem, Phys. Rev. **139**, A796 (1965).

[60] See Supplemental Material at http://link.aps.org/supplemental/10.1103/PhysRevB.105.035136 for more details. Supplementary material: Topological Luttinger semimetallic phase accompanied with surface states realized in silicon.

[61] A. A. Mostofi, J. R. Yates, G. Pizzi, Y.-S. Lee, I. Souza, D. Vanderbilt, and N. Marzari, An updated version of wannier90: A tool for obtaining maximally-localised Wannier functions, Comput. Phys. Commun. **185**, 2309 (2014).

[62] Q. Wu, S. Zhang, H.-F. Song, M. Troyer, and A. A. Soluyanov, WannierTools: An open-source software package for novel topological materials, Comput. Phys. Commun. **224**, 405 (2018).

[63] R. Haerle, E. Riedo, A. Pasquarello, and A. Baldereschi, sp^2/sp^3 hybridization ratio in amorphous carbon from C 1s core-level shifts: X-ray photoelectron spectroscopy and first-principles calculation, Phys. Rev. B **65**, 045101 (2001).

[64] M. Z. Bazant, E. Kaxiras, and J. F. Justo, Environment-dependent interatomic potential for bulk silicon, Phys. Rev. B **56**, 8542 (1997).

[65] M. Kharitonov, J.-B. Mayer, and E. M. Hankiewicz, Universality and Stability of the Edge States of Chiral-Symmetric Topological Semimetals and Surface States of the Luttinger Semimetal, Phys. Rev. Lett. **119**, 266402 (2017).

[66] P.-O. Löwdin, A note on the quantum-mechanical perturbation theory, J. Chem. Phys. **19**, 1396 (1951).

[67] H. Zhang, C.-X. Liu, X.-L. Qi, X. Dai, Z. Fang, and S.-C. Zhang, Topological insulators in Bi_2Se_3, Bi_2Te_3 and Sb_2Te_3 with a single Dirac cone on the surface, Nat. Phys. **5**, 438 (2009).

[68] Z. Wang, Y. Sun, X.-Q. Chen, C. Franchini, G. Xu, H. Weng, X. Dai, and Z. Fang, Dirac semimetal and topological phase transitions in Na_3Bi (A= Na, K, Rb), Phys. Rev. B **85**, 195320 (2012).

[69] Q. Wang, B. Xu, J. Sun, H. Liu, Z. Zhao, D. Yu, C. Fan, and J. He, Direct band gap silicon allotropes, J. Am. Chem. Soc. **136**, 9826 (2014).

[70] D. Zhang, H. Wang, J. Ruan, G. Yao, and H. Zhang, Engineering topological phases in the Luttinger semimetal α-Sn, Phys. Rev. B **97**, 195139 (2018).

[71] Z. Zhu, Y. Liu, Z.-M. Yu, S.-S. Wang, Y. X. Zhao, Y. Feng, X.-L. Sheng, and S. A. Yang, Quadratic contact point semimetal: Theory and material realization, Phys. Rev. B **98**, 125104 (2018).

[72] M. I. Aroyo, J. Perez-Mato, D. Orobengoa, E. Tasci, G. de la Flor, and A. Kirov, Crystallography online: Bilbao crystallographic server, Bulg. Chem. Commun. **43**, 183 (2011).